Modeling and Analysis of a Nonlinear Locally Resonant Metamaterial with Inductance Shunt

Arun Malla[1], Mohammad Bukhari[1], and Oumar Barry[1]

[1]VibRo Lab, Department of Mechanical Engineering, Virginia Polytechnic University, 301 Durham Hall, Blacksburg, VA, 24060

Abstract

This paper investigates a weakly nonlinear metamaterial with electromechanical local resonators coupled to a resistance-inductance shunt circuit. An analytical solution is developed for the system using the perturbation method of multiple scales, and validated through direct numerical integration. Linear and nonlinear band structures are used for parametric analysis of the system, focusing on the effect of system parameters on band gap formation and vibration attenuation. In addition, the effects of nonlinearity and the interaction with shunt parameters are examined. Results describe multiple methods of tuning band gaps and pass bands of the system through various parameters, demonstrating the flexibility and potential of the examined metamaterial.

Introduction

Metamaterials are artificially engineered structures that possess properties not found in naturally occurring materials (Hussein et al. 2014). The unusual features of metamaterials make them beneficial for numerous applications including vibration and noise control, energy harvesting, non-destructive testing, and acoustic rectifiers.

Metamaterials consist of many unit cells arranged in periodic or aperiodic patterns. It has been observed that periodic structures prevent waves from propagating through the structure at certain frequency ranges, known as band gaps (Kushwaha et al. 1993). Because these band gaps are constrained by the unit cell dimensions, the application of basic metamaterials was limited to large structures (Hussein et al. 2014). To expand the use of metamaterials to smaller components,

Liu et al. (2000) introduced local resonators, showing that locally resonant metamaterials are able to control vibrations at wavelengths much smaller than the lattice constant. Local resonators are also capable of widening the original band gap. Further manipulation of the system's band structure can also be achieved by introducing multiple resonators (Huang and Sun 2010).

Band gaps can also be affected by the incorporation of piezoelectric materials and shunt circuits. Piezoelectric materials have long been utilized in both active and passive methods for vibration control (Hagood and von Flotow 1991), and more recently have been incorporated into metamaterials (Thorp et al. 2001). By including piezoelectric elements in a metamaterial, the mechanical system dynamics can be coupled to an easily modifiable shunt circuit, enabling convenient adjustment of the metamaterial's overall properties. Incorporating piezoelectric materials and shunt circuits enables techniques such as the use of negative capacitance (Beck et al. 2011) or resonant shunt circuits (Wang and Chen 2015) to control vibrations and create or broaden band gaps. In addition, shunt circuits also offer an avenue for simultaneous energy harvesting. An important parameter in any work involving piezoelectric materials is the system's electromagnetic coupling factor. This parameter is dependent on the design and material properties of the piezoelectric component (Sugino et al. 2017). Though this piezoelectric coupling coefficient is usually on the order of 10^{-10} for engineering applications (Erturk and Inman 2011), signifying weak electromagnetic coupling, some features may only be apparent in the case of strong electromagnetic coupling.

Combining the two previously discussed methods, researchers have also investigated metamaterials with both local resonators and shunt circuits. Sugino et al. (2017) studied a locally resonant material coupled to a shunt with piezoelectric elements. This work differs from Sugino's by incorporating the piezoelectric material into the local resonators. In addition, the effects of nonlinearity and potential interactions with shunt parameters are examined. This paper applies analytical and numerical methods to investigate the effect of electromechanical coupling and shunt circuit parameters on wave propagation and energy harvesting in a nonlinear acoustic metamaterial with resistance-inductance shunt. The metamaterial is modeled through a nonlinear system of governing equations, and the perturbation method of multiple scales is utilized to derive an approximate solution. This solution is validated against the direct analytical solution for the linear case, and the directly integrated numerical results for the nonlinear case. The solution from the method of multiple scales is then used to analyze the effect of parameters on the system band structure as well as their interaction with nonlinearity, focusing on the resultant applications for simultaneous vibration control and energy harvesting.

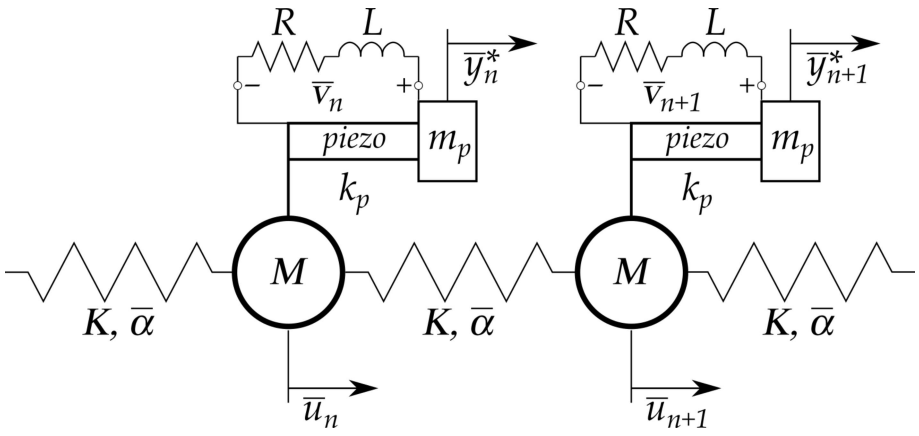

Figure 1: Schematic of nonlinear metamaterial with electromechanical resonators.

Mathematical Modeling of the System

The system studied in this work is a nonlinear acoustic metamaterial coupled with electromechanical local resonators. The metamaterial consists of a chain of cells connected by nonlinear springs as shown in Figure 1. Each nonlinear spring has linear spring coefficient K and nonlinear spring coefficient $\bar{\alpha}$. Each resonator consists of a substrate covered by a piezoelectric layer, with total effective mass m_p and effective linear stiffness k_p. The piezoelectric layer is shunted to a resistance-inductance (RL) circuit as shown in Figure 1. This circuit has voltage difference $\bar{v}_n$, resistance R, and inductance L. The piezoelectric layer has capacitance C_p and electromechanical (EM) coupling coefficient θ. The absolute displacement of cell n is $\bar{u}_n$, and the absolute displacement of the attached piezoelectric resonator is $\bar{y_n}^*$.

Following Bukhari and Barry (2020), we introduce nondimensional variables: $u_n = \bar{u}_n/U_0$, $y_n = \bar{y}_n/U_0$, and $v_n = \bar{v}_n/V_0$, where U_0 and V_0 are initial displacement and velocity, respectively. Here, $\bar{y}_n = \bar{y}_n^* - \bar{u}_n$ is the relative displacement of piezoelectric local resonator n with respect to cell n. We also introduce nondimensional time $\tau = \omega_n t$, where

$$\omega_n = \sqrt{K/M} \tag{1}$$

is the mechanical natural frequency of a unit cell.

With these variables, the normalized coupled equations of motion for each cell, local resonator, and shunt circuit can be written for an infinite chain as:

$$\ddot{u}_n + 2u_n - u_{n+1} - u_{n-1} + \alpha(u_n - u_{n+1})^3 + \alpha(u_n - u_{n-1})^3 + \bar{k}\Omega_1^2(\ddot{u}_n + \ddot{y}_n) = 0 \tag{2}$$

$$\Omega_1^2\ddot{y}_n + y_n - \alpha_1(\alpha_3\dot{v}_n + v_n) = -\Omega_1^2\ddot{u}_n \tag{3}$$

$$\Omega_2^2\ddot{v}_n + \alpha_2\dot{v}_n + v_n + \alpha_4\dot{y}_n = 0 \tag{4}$$

where $\alpha = \bar{\alpha}U_0^2/K$, $\Omega_1 = \omega_n/\omega_p$, $\omega_p = \sqrt{k_p/m_p}$, $\bar{k} = k_p/K$, $\alpha_1 = \theta V_0/k_p U_0$, $\alpha_3 = L\omega_n/R$, $\Omega_2 = \omega_n/\omega_e$, $\omega_e^2 = 1/\sqrt{LC_p}$, $\alpha_2 = RC_p\omega_n$, and $\alpha_4 = R\theta\omega_n U_0/V_0$.

To develop an approximate solution of the nonlinear governing equations of motion Eqs. (2)-(4), the perturbation method of multiple scales is utilized. This method is described in the following section.

Solving With Method of Multiple Scales

The perturbation method of multiple scales (MMS) is carried out following the procedure outlined by Nayfeh (2011). First we introduce a small dimensionless parameter ϵ ($\epsilon \ll 1$) in the governing equations by defining multiple time scales:

$$T_0 = \tau\,, \quad T_1 = \epsilon\tau \tag{5}$$

where T_0 is the fast time scale and T_1 is the slow time scale. The time derivative operators are then perturbed and can be expressed as

$$\frac{\delta}{\delta\tau} = D_0 + \epsilon D_1 + O(\epsilon^2) \tag{6a}$$

$$\frac{\delta^2}{\delta\tau^2} = D_0^2 + 2\epsilon D_0 D_1 + O(\epsilon^2) \tag{6b}$$

where $D_n = \delta/\delta T_n$. Following this, the solutions of the nonlinear governing equations of motion (Eqs. (2) - (4)) can be expressed as power series in powers of ϵ as

$$u_n(\tau) = u_{n,0}(T_0, T_1) + \epsilon u_{n,1}(T_0, T_1) + O(\epsilon^2)\,, \tag{7a}$$

$$y_n(\tau) = y_{n,0}(T_0, T_1) + \epsilon y_{n,1}(T_0, T_1) + O(\epsilon^2)\,, \tag{7b}$$

$$v_n(\tau) = v_{n,0}(T_0, T_1) + \epsilon v_{n,1}(T_0, T_1) + O(\epsilon^2)\,. \tag{7c}$$

The governing equations are converted into a weakly nonlinear form by rescaling the parameter $\alpha = \alpha\epsilon$. Through introducing this substitution and Eqs. (5)–(7) into Eqs. (2)–(4), then collecting different orders of ϵ we get the linear and nonlinear problems.

For $\mathcal{O}(\epsilon^0)$ terms, the problem is linear. Thus, the solution can be expressed as:

$$u_{n,0}(T_0) = Ae^{i(nk-\omega T_0)} + c.c. \tag{8a}$$

$$y_{n,0}(T_0) = Be^{i(nk-\omega T_0)} + c.c. \tag{8b}$$

$$v_{n,0}(T_0) = Ce^{i(nk-\omega T_0)} + c.c. \tag{8c}$$

where k is the wavenumber and ω is the linear frequency normalized by mechanical natural frequency ω_n. A, B, and C are functions of the slow time scale T_1, and $c.c.$ denotes the complex conjugate of the preceding term.

Solving the linear problem gives B and C in terms of A:

$$C = \Gamma_1 B \tag{9}$$

$$B = \Gamma_2 A \tag{10}$$

as well as the linear dispersion relation:

$$-\omega^2 + 2 - 2cos(k) - \Omega_1^2 \bar{k} \omega^2 (1 + \Gamma_2) = 0 \tag{11}$$

where Γ_1 and Γ_2 are functions of ω^2 and various parameters.

Solving Eq. (11) reveals six roots for ω in the form of three complex conjugate pairs. Consequently, the band structure may have up to three pass bands depending on the system parameters.

Collecting $\mathcal{O}(\epsilon^1)$ terms provides the nonlinear problem, which can be used to determine $A(T_1)$. The polar form of $A(T_1)$ is defined as:

$$A(T_1) = \frac{1}{2} a(T_1) e^{ib(T_1)} \tag{12}$$

Solving for a and b yields the equations:

$$ga' + hab' + f = 0 \tag{13}$$

$$-ha' + gab' + l = 0 \tag{14}$$

where g, h, f,and l are functions of ω and system parameters. Here, prime ($'$) denotes the derivative with respect to T_1.

Eqs. (13) and (14) can then be solved for the slow flow equations:

$$a' = c_0 a^3 \tag{15}$$

$$b' = c_1 a^2 \tag{16}$$

where c_0 and c_1 are functions of g, h, f,and l. By comparing the values of c_0 and c_1, it can be observed that the magnitude of c_0 is extremely small compared to that of c_1. Therefore, it can be assumed negligible, $c_0 \approx 0$. This gives $a' = 0$ and $a(T_1) =$ a constant a_0. Thus, the nonlinear frequency correction factor is:

$$b' = c_1 a_0^2 \tag{17}$$

and the nonlinear frequency is:

$$\omega_{NL} = \omega - \epsilon b' \tag{18}$$

Integrating Eq. (17) yields the approximate solution for $b(T_1)$:

$$b = c_1 a_0^2 T_1 \tag{19}$$

The linear and nonlinear dispersion curves derived by the method of multiple scales are then validated against a numerical solution and used to conduct band structure analysis of the system.

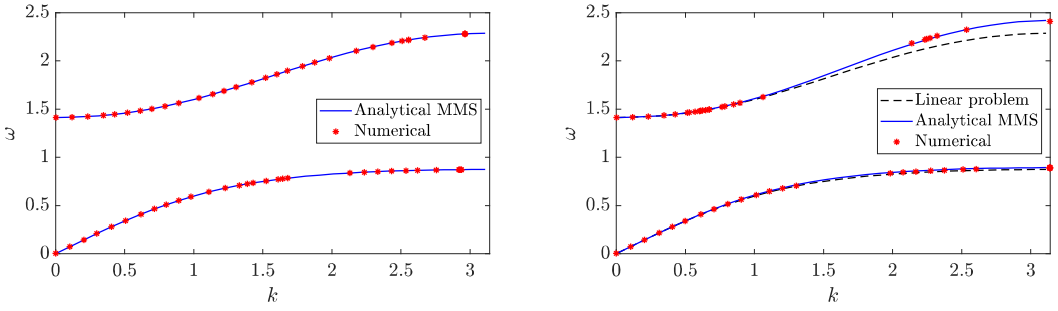

(a) (b)

Figure 2: Validation of numerical and analytical results; (a) Linear problem, $\epsilon\alpha a_0^2 = 0$; (b) Nonlinear problem, $\epsilon\alpha a_0^2 = 0.06$.

Band Structure Analysis

0.1 Validation

To validate the linear and nonlinear dispersion relations, they are compared to a numerical simulation of the system. The system is as described in Figure 1, with 500 cells coupled to electromechanical resonators with RL shunt circuits. Cells are connected with both linear and nonlinear springs. Shunt parameter values are: $R = 10^3\ \Omega$, $L = 0.2212$ H, and $C_p = 1.13e\text{-}10$ F. The mass of each main cell is $M = 0.125$ kg, and the mass ratio between each piezeoelectric resonator and main cell is $m_p/M = 0.1$. The mechanical and electrical resonance frequencies of the resonator, ω_p and ω_e, are tuned such that $\omega_n = \omega_p = \omega_e = 2e5$ rad/s. These parameters are chosen based on the similar system examined by Abdelmoula and Abdelkefi (2015). The case of weak EM coupling $\theta = 110$ N/V is considered.

Following the similar procedure described by Bukhari and Barry (2020), the system is validated by exciting the chain with a transient wave packet and numerically integrating the governing equations using the built-in MATLAB solver ode45. For a given wavenumber, the system is simulated for a long time to allow the wave to propagate through the chain. After this, a 2D Fast Fourier transform (2DFFT) is applied to the time data collected in the wavenumber and frequency domains. The transformed data is then used to determine the natural frequency of the system by finding the frequency associated with the maximum power density point. By determining the natural frequencies corresponding to a range of wavenumbers over the first Brillouin zone, the dispersion curves are numerically constructed and compared to the analytical solution in Figure 2, which plots normalized frequency ω against wavenumber k.

Both linear and nonlinear dispersion relations are compared in Figure 2. These comparisons show good agreement between analytical and numerical solutions for both the linear and nonlinear dispersion relations. It should be noted that the

numerical solution is unable to capture certain frequencies of the nonlinear solution in the medium and short wavelength limits for both branches. These areas, known as pseudo band gaps, are due to a significant frequency shift associated with transient wave packet excitation (Zhou et al. 2018). When excited within these pseudo band gaps, the solution appears instead at frequencies within the long and short wavelength limits.

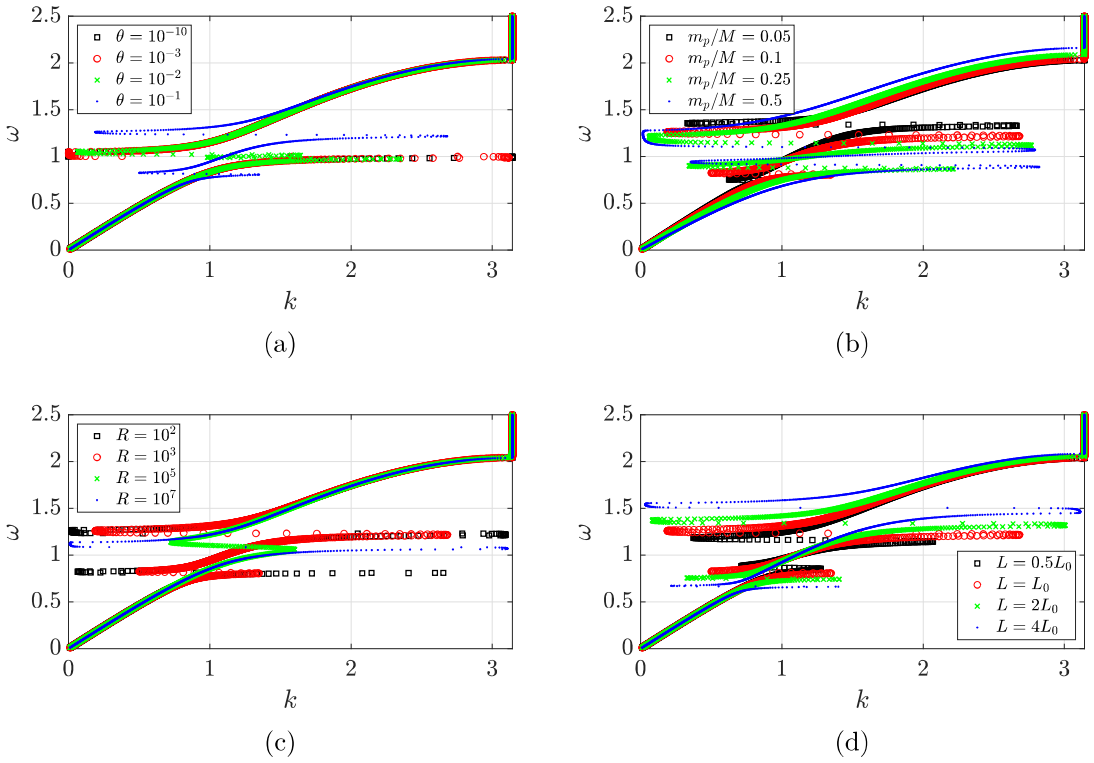

Figure 3: Effect of system parameters on linear band structure, $\omega_e = \omega_n$: (a) Effect of EM coupling, $m_p/M = 0.1$, $R = 10^3\ \Omega$, $L = 0.2212$ H; (b) Effect of resonator/main cell mass ratio, $\theta = 10^{-1}$ N/V, $R = 10^3\ \Omega$, $L = 0.2212$ H; (c) Effect of shunt resistance, $\theta = 10^{-1}$ N/V, $m_p/M = 0.1$, $L = 0.2212$ H; (d) Effect of shunt inductance, $\theta = 10^{-1}$ N/V, $m_p/M = 0.1$, $R = 10^3\ \Omega$.

Linear Band Structure

Next, the validated analytical dispersion relations are used to study the effect of selected parameters on the band structure, beginning with the linear dispersion relation calculated using Eq. (11). The parameters examined are EM coupling coefficient θ, the mass ratio between the piezoelectric resonator and main cell m_p/M, shunt resistance R, and piezoelectric capacitance C_p. Unless otherwise noted, parameter values are the same as in Section 0.1. Comparisons are also made to the band structure of

the system examined by Bukhari and Barry (2020), which is similar except for the absence of inductor in the shunt circuit.

Varied EM coupling is shown in Figure 3(a), with the value of θ ranging from weak EM coupling at $\theta = 1e\text{-}10$ N/V to strong EM coupling at $\theta = 1e\text{-}1$ N/V. For weak coupling values, $\theta = 1e\text{-}10$ to $1e\text{-}3$ N/V, the coupling has minimal effect on the band structure, which is similar to the case of resistance-only shunt circuit in Bukhari and Barry (2020). However, at $\theta = 1e\text{-}2$ N/V, a third mode branch can be observed forming between the acoustic and optical modes. Instead of a single band gap, two smaller band gaps are formed. These effects are more visible for $\theta = 1e\text{-}1$ N/V.

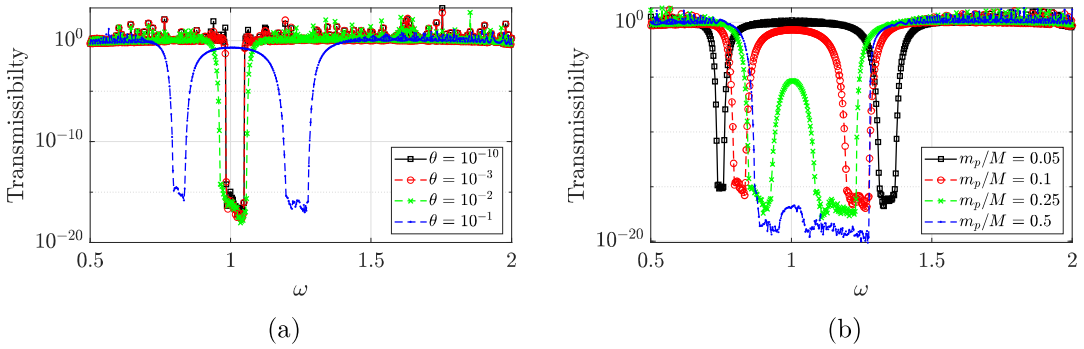

Figure 4: Effect of system parameters on transmissibility, $\omega_e = \omega_n$, $R = 10^3$ Ω, $L = 0.2212$ H: (a) Effect of EM coupling, $m_p/M = 0.1$; (b) Effect of resonator/main cell mass ratio, $\theta = 10^{-1}$ N/V.

Figure 3(b) displays the effects of varying the mass ratio between the piezoelectric resonator and main cell. Here, the main cell mass is kept fixed at $M = 0.125$ kg and the resonator mass is altered to meet the desired ratio. In addition to band gap location, resonator mass has a clear effect on the width of the band gaps between the modes, with the band gaps broadening as resonator mass increases. This is consistent with the effects of mechanical-only resonators, which are well established in the literature (Inman 1994). These broadening band gaps effect the middle mode branch, which becomes increasingly narrow as mass ratio increases. In addition, the upper boundary of the acoustic mode significantly increases with mass ratio.

The effects of shunt resistance are shown in Figure 3(c). It is clear that this value effects the formation of the central mode branch. At low resistance values $R = 10^2$ to 10^3 Ω, all three modes are present, but the central branch merges back into the acoustic and optical modes as resistance increases. This high resistance case is near identical to the band structure with resistance-only shunt studied by Bukhari and Barry (2020). Due to this observation regarding the effect of high shunt resistance, $R = 10^3$ Ω for all following analysis. In Figure 3(d), varied shunt inductance is examined. Due to the electrical resonance frequency being fixed at $\omega_e = 1/\sqrt{LC_p} = \omega_n$, increasing L means decreasing C_p and vice versa. Increasing L

results in the central mode branch becoming broader as the band gaps move apart.

To supplement the study of the linear band structure, frequency response functions (FRFs) are also obtained through direct numerical simulation of the 500-cell metamaterial chain system. The transmissibility of the chain for each frequency is determined by comparing the output power harvested by the 500th cell to the input power at the 1st cell:

$$H_p = \frac{\int_0^{t_f} P_{out}(t)dt}{\int_0^{t_f} P_{in}(t)dt} \tag{20}$$

where $t_f = 3000$ s. The resulting FRFs, shown in Figure 4, support the observations drawn from the band structure analysis while also making other details more apparent.

Figure 4(a), displaying the effects of θ, shows similar results to the band structure in Figure 3(a), with the band gap remaining consistent from $\theta = 1e$-10 to $1e$-3 N/V, and splitting into two at $\theta = 1e$-1 N/V. However, at $\theta = 1e$-2 N/V, the band gap broadens, but the central mode branch is not yet visible. This suggests that the mode branch is too narrow to be visible, or that there is no significant difference in vibration propagation between the mode and the band gaps for this value of θ. Another notable observation is the transmissibility of the central mode branch at strong coupling, $\theta = 1e$-1 N/V. While waves certainly propagate with higher amplitude in the mode than the band gaps, the transmissibility is also significantly less than in the acoustic and optical modes. In addition, transmissibility drops off gradually as the band gaps are approached, unlike the lower-coupling cases. Similar observations are made by varying mass ratio, shown in Figure 4(b)

Nonlinear Band Structure

The nonlinear band structure is also studied by taking into account the correction factor defined by Eq. (18). The nonlinear stiffness parameter $\epsilon\alpha A^2$ is varied to model chains with nonlinear hardening ($\epsilon\alpha A^2 = 0.03$) and nonlinear softening ($\epsilon\alpha A^2 = -0.03$). The effects of nonlinear hardening and softening are then combined with the effects of EM coupling, mass ratio, and shunt inductance by varying selected parameters.

The effect of nonlinear hardening or softening on the dispersion curves with default parameters is shown in Figure 5(a). As expected, hardening shifts the curves up on the frequency axis, while softening shifts them down. The magnitude of the shift is negligible for small wavenumber (long wavelength limit), and more pronounced for the optical mode branch, especially at large wavenumber (short wavelength limit). For the acoustic mode branch and central mode branch, the effects of nonlinearity are largest around the medium wavelength region, but decrease near the end of each mode. Thus, the effect on bandgap boundaries is present, but minimal. However, the upper bound of the optical mode, where nonlinearity has prominent effect, is significantly shifted.

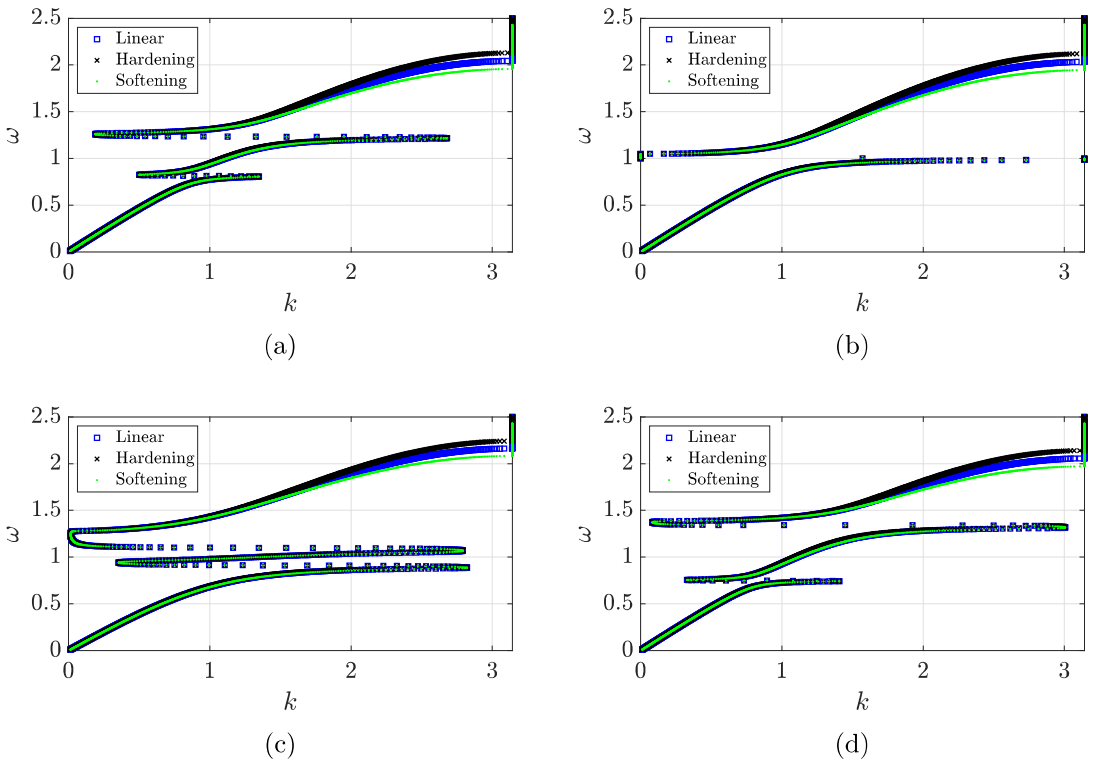

Figure 5: Effect of system parameters on nonlinear band structure for: (a) Default parameters; (b) Weak EM coupling $\theta = 10^{-10}$ N/V; (c) Large mass ratio $m_p/M = 0.5$; (d) Shunt inductance $L = 2L_0$.

The cases of linear and nonlinear chains with weak EM coupling are displayed in Figure 5(b). Here, the shifts of the cutoff frequencies due to nonlinear hardening and softening are largely the same as the case of strong coupling. The band structure has two branches rather than three, matching the effects of weak coupling previously established. Again, the bounds at the top of the acoustic mode and the bottom of the optical mode are not significantly affected by nonlinearity, with larger effects visible at the upper bound of the optical mode. Similar results are seen when altering the mass ratio, as displayed in Figure 5(c). As expected from the linear analysis, the central mode branch becomes narrow, and band gaps are broader than the default case. The effects of nonlinearity also become slightly more prominent in the acoustic mode, and remain significant in the optical mode.

Finally, the shunt inductance is increased to $L = 2L_0$ in Figure 5(d). As noted in Figure 3(d), this results in the central mode branch occupying a larger frequency range than the default case in Figure 5(a). Due to this, the effects of nonlinearity are more prominent for this mode, especially in the medium wavelength region. However, effects of nonlinearity still decrease in the short wavelength region, reducing the effect on the band gap boundary.

Conclusions

This work contains the analysis of a nonlinear, electromechanical metamaterial coupled to a shunt circuit with both resistor and inductor. The system consists of a chain of cells connected by nonlinear springs, with each cell coupled to an electromagnetic resonator consisting of piezoelectric element and shunt circuit. Both the cells and resonators were modeled as spring-mass systems, with the resonator system coupled to the dynamics of the shunt circuit. The resulting governing equations were solved analytically using the perturbation method of multiple scales, and the approximate solution was validated by direct numerical integration. The validated analytical solutions were then used to examine the system's band structure to view the effect of electromagnetic coupling and resonator parameters including mass ratio, shunt resistance, and shunt inductance. For the linear case, band structure analysis was also supported by transmissibility diagrams obtained by solution of the linear system equations. Focus was given to manipulating band gaps and the system's mode branches through resonator parameters, and the resulting effects on vibration attenuation within the chain.

In this paper, several notable observations were made concerning shunt parameters. It was shown that using strong EM coupling and low resistance, a band structure with three pass bands can be obtained, rather than the two pass band structure from low EM coupling or resistance-only shunt. The effects of nonlinear springs on the system dynamics, especially the interaction with the resonator and shunt parameters, were also studied. With the insight gained from the parametric study in this work, there is great potential for optimizing both vibration control and energy harvesting in this and similar metamaterials.

References

Abdelmoula, H. and Abdelkefi, A. (2015). "Ultra-wide bandwidth improvement of piezoelectric energy harvesters through electrical inductance coupling." *The European Physical Journal Special Topics*, 224, 2733–2753.

Beck, B. S., Cunefare, K. A., Ruzzene, M., and Collet, M. (2011). "Experimental analysis of a cantilever beam with a shunted piezoelectric periodic array." *Journal of Intelligent Material Systems and Structures*, 22, 1177–1187.

Bukhari, M. A. and Barry, O. (2020). "Simultaneous energy harvesting and vibration control in a nonlinear metastructure: A spectro-spatial analysis." *Journal of Sound and Vibration*, 473, 115215.

Erturk, A. and Inman, D. J. (2011). *Piezoelectric energy harvesting*. John Wiley & Sons.

Hagood, N. W. and von Flotow, A. (1991). "Damping of structural vibrations with piezoelectric materials and passive electrical networks." *Journal of Sound and Vibration*, 146(2), 242–268.

Huang, G. and Sun, C. (2010). "Band gaps in a multiresonator acoustic metamaterial." *Journal of Vibration and Acoustics*, 132(3), 031003.

Hussein, M. I., Leamy, M. J., and Ruzzene, M. (2014). "Dynamics of phononic materials and structures: Historical origins, recent progress, and future outlook." *Applied Mechanics Reviews*, 66(4), 040802.

Inman, D. J. (1994). *Engineering vibration*. Prentice Hall.

Kushwaha, M. S., Halevi, P., Dobrzynski, L., and Djafari-Rouhani, B. (1993). "Acoustic band structure of periodic elastic composites." *Physical review letters*, 71(13), 2022.

Liu, Z., Zhang, X., Mao, Y., Zhu, Y., Yang, Z., Chan, C. T., and Sheng, P. (2000). "Locally resonant sonic materials." *science*, 289(5485), 1734–1736.

Nayfeh, A. H. (2011). *Introduction to perturbation techniques*. John Wiley & Sons.

Sugino, C., Leadenham, S., and Ruzzene, M. (2017). "An investigation of electroelastic bandgap formation in locally resonant piezoelectric metastructures." *Smart Materials and Structures*, 26, 055029.

Thorp, O., Ruzzene, M., and Baz, A. (2001). "Attenuation and localization of wave propagation in rods with periodic shunted piezoelectric patches." *Smart Materials and Structures*, 10(5), 979.

Wang, G. and Chen, S. (2015). "Large low-frequency vibration attenuation induced by arrays of piezoelectric patches shunted with amplifier-resonator feedback circuits." *Smart Materials and Structures*, 25, 331–346.

Zhou, W. J., Li, X., Wang, Y., Chen, W., and Huang, G. (2018). "Spectro-spatial analysis of wave packet propagation in nonlinear acoustic metamaterials." *Journal of Sound and Vibration*, 413, 250–269.